

A Robust Filter for Marker-less Multi-person Tracking in Human-Robot Interaction Scenarios

Enrico Martini^{1,2*}, Harshil Parekh², Shaoting Peng², Nicola Bombieri¹, and Nadia Figueroa²

Abstract—Pursuing natural and marker-less human-robot interaction (HRI) has been a long-standing robotics research focus, driven by the vision of seamless collaboration without physical markers. Marker-less approaches promise an improved user experience, but state-of-the-art struggles with the challenges posed by intrinsic errors in human pose estimation (HPE) and depth cameras. These errors can lead to issues such as robot jittering, which can significantly impact the trust users have in collaborative systems. We propose a filtering pipeline that refines incomplete 3D human poses from an HPE backbone and a single RGB-D camera to address these challenges, solving for occlusions that can degrade the interaction. Experimental results show that using the proposed filter leads to more consistent and noise-free motion representation, reducing unexpected robot movements and enabling smoother interaction.

I. INTRODUCTION

In recent years, integrating robots into homes, offices, and public spaces has become increasingly common, changing the dynamics of Human-Robot Interaction (HRI) and making it more important to ensure that these interactions remain safe and robust. The robot’s knowledge of its environment is an essential component of this coexistence.

Traditional HRI tasks (e.g., collision avoidance [1] and teleoperations [2]) have heavily relied on marker-based motion capture systems to detect human poses for their high precision and low latency. Such systems use reflective markers to accurately track human movements [3], [4], detected by multiple fixed high-speed cameras, achieving speeds up to 250Hz with sub-millimeter errors [5]. However, the intrusiveness, limited mobility, and cost implications associated with marker-based motion capture systems preclude their integration into everyday human-robot interaction tasks at the consumer level.

In contrast, marker-less motion tracking represents a leap towards more natural and unobtrusive human-robot interactions [6], providing a cheap and easy solution. Human pose estimation (HPE) is a computer vision task that involves determining the position of a person’s joints from images or videos. Recent advances in deep learning algorithms have

greatly improved performance and robustness, making it a rapidly evolving area of research [7]. Previous works [8], [9] combined RGB-D cameras and HPE to interpret human motions in 3D. Still, performance falls short as errors increase along with the distance from the camera [10]. In dynamic environments, where humans and robots coexist, there are even more limitations regarding accuracy, real-time processing, and handling occlusions or complex human poses [6]. While some research [11], [12], [13] attempt to use marker-less human-pose detections, they employ multiple sensors [14]. In the context of HRI, most approaches prefer marker-based solutions due to the quality of measurement [15] and frequency of data which makes reactive motion policies possible [16]. In [17], [18], authors used a single camera and an HPE to demonstrate the desired end-effector movement of a robotic arm. Both approaches are designed for single-person and avoid simultaneous robot and human movement. All these approaches do not consider missing data information and large errors, which often occur in real-world scenarios and can degrade the estimation results. A multi-person collaborative scenario is even more prone to error because the HPE may not detect body parts occluded by the robot, objects, and other people; interactions between people, overlapping body parts, and self-occlusions further degrade poses [19].

To overcome these limitations, we propose a novel filtering pipeline that can provide a reliable target for the robot to handle multiple people in a close environment from a single camera. Since it only takes a set of 3D skeletons and the prediction confidence as input, it can be combined with any existing HPE backbone. Figure 1 shows our filter, consisting of three steps: a spatial node, a temporal node, and a permanence filter node. The spatial node determines whether each prediction is reliable based on the spatial relationship between detected human joints. The temporal node tracks the people in the scene and assigns a unique label to each prediction based on the position of each body joint and the reliability of the prediction. The filter node leverages the information from the previous nodes to detect occlusions and make smooth predictions even in prolonged and complete occlusions.

We tested the proposed pipeline in a multi-person scenario on four tasks of increasing complexity with seven different operators. Each task, described in Figure 2, emulates real-world actions, such as inspections and handovers of light and heavy objects. The robot closely follows the operator’s left wrist while another human collaborates with the operator, simulating the learning task from human-human interactions.

This work has been supported by the "PREPARE" project (n. F/310130/05/X56 - CUP: B39J23001730005) - D.M. MiSE 31/12/2021, and the PNRR research activities of the consortium iNEST (Interconnected North-Est Innovation Ecosystem) funded by the European Union Next-GenerationEU (Piano Nazionale di Ripresa e Resilienza (PNRR) – Missione 4 Componente 2, Investimento 1.5 –D.D. 1058 23/06/2022, ECS 00000043). This manuscript reflects only the Authors’ views and opinions, neither the European Union nor the European Commission can be considered responsible for them.*Corresponding author: enrico.martini@univr.it

¹Department of Engineering for Innovation Medicine, University of Verona, Verona, Italy.

²GRASP Lab, Department of Mechanical Engineering and Applied Mechanics, University of Pennsylvania, Philadelphia, USA.

We compared our filter with two Kalman filter variants that work in real-time and OpenPose [20], assumed as a baseline. Comparing the results of these methods with a marker-based motion capture system used as ground truth shows that the proposed filter outperforms the other methods in all tasks. Furthermore, we monitored the safety distance between the robot and the operator’s hand. We asked all study participants to rate on a Likert scale how safe and comfortable the interaction felt. Our method provided the safest and smoothest interaction with the least variability in the safety distance, surpassing traditional tracking algorithms. The code is publicly available at <https://github.com/penn-figueroa-lab/markerless-human-perception>.

II. FILTERING PIPELINE

We propose a plug-and-play filter that smoothes and tracks human poses estimated by any Multi-Person HPE to enable easier cooperation between humans and robots. Figure 1 shows an overview of the pipeline. A calibrated camera provides the RGB image, depth matrix, and intrinsics (i.e., focal length and principal points) to the HPE module. All HPE platforms rely on neural networks, but some infer the keypoints directly in 3D space [21], while others provide 2D keypoints that are projected in 3D using the depth matrix [20], [22]. Either way, the result is a set of skeletons S_k , where each skeleton $s_k \in S_k$ contains the 3D keypoints (i.e., coordinates of the human joints) extrapolated from an image, along with the confidence of the prediction. All those neural networks are trained on large generic datasets containing annotated images or videos of multiple people in various poses. When applied to an environment not present in the training dataset, such as an industrial plant, raw predictions are often inaccurate, with missing or misplaced keypoints, affecting HRI feasibility. Our solution to improve the outcome of generic backbones consists of a plug-and-play filter composed of a spatial evaluation module, a temporal evaluation and tracking module, and a permanence filter. The following sections describe each block in more detail.

A. Spatial Evaluation

This module determines whether to increase or decrease the confidence of each prediction based on the spatial relationship between keypoints, and the relationship between the skeleton and the camera. Each skeleton that enters this module is represented as a set of labeled 3D keypoints, each one defined as:

$$\text{kp}_{i,k} = [x, y, z, c] \quad (1)$$

where x, y, z is the 3D position in the camera frame of keypoint i at time k , and c is the confidence of the prediction from the HPE. To fully evaluate spatial properties, we build a direct acyclic graph (DAG), where each keypoint is a node, and each link between two adjacent keypoints is represented as an edge. Various HPE backbones produce different keypoints, so to make our method effective, we add keypoints at strategic locations to construct the DAG, if not present. For instance, consider a simple HPE that outputs only the 12 basic keypoints (shoulders, hips, elbows, wrists,

knees, and ankles). We construct the central keypoint (i.e., the root) by averaging the position of the shoulders and hips.

We then consider the Euclidean distance between the root of each skeleton and the camera position. The skeleton is discarded if the distance exceeds a certain threshold (i.e., Δ). This is because even the newest depth sensors are subject to error, and the signal-to-noise ratio decreases significantly as the distance from the camera increases. In addition, each neural network must resize the input images to make them the same size as those used during training. This often leads to hallucinations and general inaccuracy in detecting people at long distances.

The height of the corresponding human is then estimated for each skeleton. Biomechanics and anthropometry studies have shown a well-defined relationship between segment length and human height [23]. These segment proportions are a good approximation [24], so we use them to estimate the subject’s height based on the distance between joints. For example, knowing that the forearm is 0.146 times the height, if the measured distance between the elbow and wrist is 0.25 m, the height is approximately 1.71 m. Each arc of the DAG is used to derive a height hypothesis in the height estimation process. All possible heights are filtered and averaged to estimate a plausible height.

Then, for each arc of the DAG, if its length is compatible with the estimated height, the confidence of its two keypoints is increased by a reward factor r . Conversely, if the arc’s length is incorrect, the keypoint’s confidence is decreased by a penalty factor p . If it is connected to two invalid bones, it is penalized by $2p$ because it’s probably a false detection. On the other hand, if all bones connected to a keypoint are valid, the keypoint is likely to be correctly detected by the HPE, so its confidence increases by a $2r$ factor.

B. Temporal Tracking and Evaluation

This module assigns a unique label to each skeleton to keep track of the people in the scene. We solve the problem using the *Hungarian method* [25], an optimization algorithm that is specifically designed for the assignment problem. Given a $n \times m$ cost matrix $M \in N^+$, where n is the number of skeletons detected at time $k - 1$ and m is the number of skeletons detected at time k , the Hungarian method finds an assignment between the n old skeletons and the m new skeletons to minimize the total cost of the assignment. Typically, the cost matrix used for tracking 3D point clouds is constructed by computing the Euclidean distance between the centroids of each point cloud [26]. This is more complex with skeletons because the number of points is small and variable. In this context, it is necessary to find a robust cost matrix to make the Hungarian method effective.

First, we build a distance score matrix D based on the Euclidean distance. Given two skeletons $s_{i,k-1}$ and $s_{j,k}$, the average of the distance of common keypoints between $s_{i,k-1}$ and $s_{j,k}$ is stored in $D_{i,j}$. If two sets of keypoints are disjointed, $D_{i,j}$ is left empty. At the end of the computation, all empty cells are filled with the highest element $\max(D)$. At the same time, we build a confidence score matrix C .

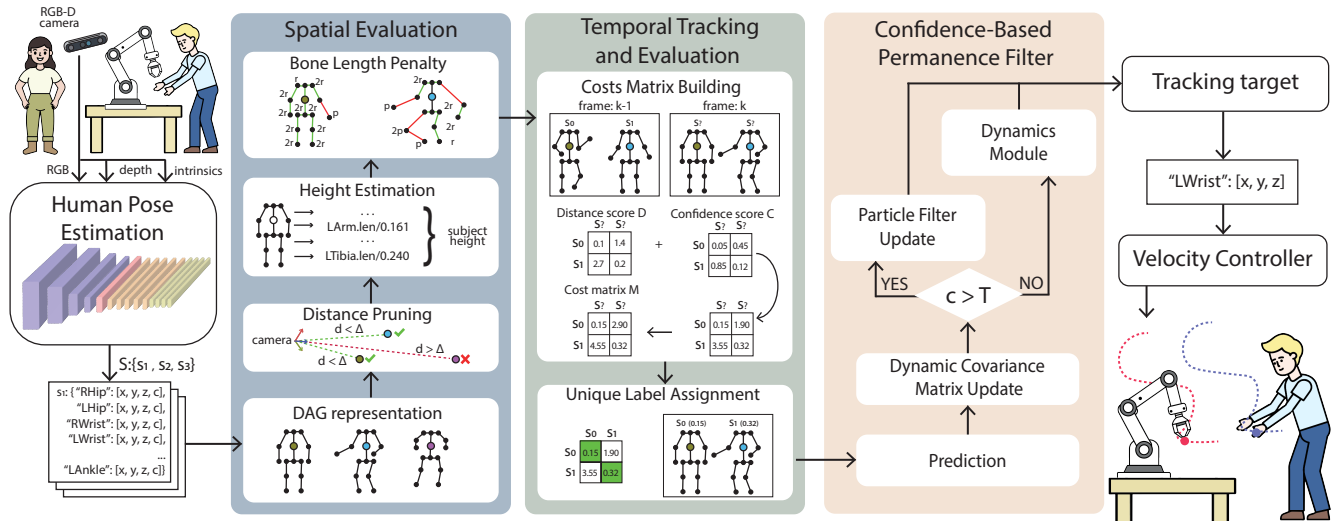


Fig. 1: The proposed filter overview: a single camera sends the stream of a multi-person HRI scenario to a generic HPE backbone that outputs a set of 3D poses. The spatial evaluation node adjusts the initial prediction confidence based on the spatial relationship between keypoints. The temporal tracking and evaluation node assigns a unique label to each person in the scene, consistent across frames. The permanence filter uses previous trajectories to detect occlusions in the scene. This results in a refined set of skeletons fed into a tracking target node that provides the 3D position goal for the velocity controller.

Position $C_{i,j}$ stores the mean absolute distance between the confidences of $s_{i,k-1}$ and $s_{j,k}$. In disjointed sets of keypoints, C follows the same rules applied to D .

Matrices D and C are then combined to obtain matrix M such that:

$$M_{i,j} = D_{i,j} + C_{i,j} + u(D_{i,j} + C_{i,j} - \delta) \quad (2)$$

where $u(\cdot)$ is the unit step function and δ is a fixed step constant. The unit step function increases the assignment cost between skeletons whose combined score is more than δ .

The cost matrix M is then fed into a linear sum assignment solver to obtain the label assignments that minimize the total cost. Using M instead of D makes the assignment more robust to occlusions and difficult scenarios, such as intersecting people and partially visible body parts.

Once the assignment is performed, each skeleton s_j is enriched with the cost of its assignment $M_{i,j}$, useful for the permanence filter.

C. Confidence-Based Permanence Filter

When using a single camera, occlusions often occur during collaborative tasks, undermining the outcome of the interaction. To address this problem, the final node of the proposed pipeline smooths keypoints even during prolonged and complete occlusions.

The filter core is based on the Object Permanence Filter (OPF) [27], a state-observer originally designed to smooth objects' trajectories. Similar to a particle filter, the prediction step is defined as:

$$s_{k+1|k}^{(i)} = f(s_{k|k}^{(i)}, u_k) + \epsilon_k, \quad \epsilon_k \sim N(0, Q) \quad (3)$$

where the state $s = [x, y, z] \in \mathbb{R}^3$ is the cartesian position of the keypoint, $s_{k+1|k}^{(i)}$ is the state of the i^{th} keypoint in

timestamp $k + 1$ given the past k measurements, $f(\cdot)$ is the state dynamics function, and Q is the covariance of the process noise.

After the prediction step, if the measurement confidence of the keypoint is higher than the occlusion threshold T , then the correction step is performed by the *particle filter update*:

$$w_{k+1|k+1}^{(i)} = \eta P(y_{k+1}|x_{k+1|k}^{(i)}) w_{k+1|k}^{(i)} \quad (4)$$

where η is a normalization factor, and $P(y_{k+1}|x_{k+1|k}^{(i)})$ is a Gaussian that represents how the particles approximate the true object state. It is defined as:

$$P(y_{k+1}|x_{k+1|k}^{(i)}) = \frac{1}{\sqrt{(2\pi)^p \det(R)}} \exp\left(-\frac{\nu_{k+1}^T R^{-1} \nu_{k+1}}{2}\right) \quad (5)$$

where ν_k is a Gaussian observation noise and R is the measurement noise covariance matrix. Due to the probabilistic nature of neural networks, the noise level of the keypoints may significantly change. The proposed filter is aware of this, so it changes R dynamically, depending on the keypoint confidence:

$$R_{i,k} = \alpha^{c_{i,k}} - \beta \quad (6)$$

where α and β are fixed parameters. In this case, when the measurement confidence is low, the covariance is high, resulting in a larger search area; if the measurement confidence is high, the covariance is low, which indicates a more conservative state update. If a keypoint does not have any measurement available, or the confidence of the measurement is below the occlusion threshold T , the *dynamics module* models the dynamics of the keypoint under occlusion. This module approximates the motion under occlusion by fitting a first-order polynomial using the stored length trajectory γ .

At the end of this phase, the skeletons are refined and transmitted to the *tracking target*, a node that selects which wrist to follow and sends its position to the velocity controller.

III. EXPERIMENTS

A. Experimental Setup

We chose the Intel Realsense D455 for the RGB-D camera, providing $848 \times 480 @ 30$ Hz matrices on both RGB and depth streams. For the HPE backbone, we used OpenPose [20], one of the most known 2D multi-person HPEs. The 3D skeletons are obtained by re-projecting the 2D poses into the 3D camera space, as in [28]. We tracked the operator’s left wrist using a marker-based motion capture system (OptiTrack), considered ground truth. We calibrated both the robot and the camera with the Kabsch algorithm [29], aligning them with the frame defined by the OptiTrack system. The experiment runs on 2 PCs with an Intel 12700K and RTX 3090 GPU. One controls the robot and the camera stream, while the other runs the HPE backbone and the filters. Each block in Figure 1 is implemented as a ROS node and runs in real-time at 30 Hz. For the robot, we used the *Franka Emika Panda*, a 7-DOF robotic arm designed for collaborative tasks. We employ a passive velocity controller τ_c as defined in [30]. Given the joint state variable ξ , with velocity $\dot{\xi}$, and acceleration $\ddot{\xi}$, the robot has the following rigid-body dynamics:

$$M(\xi)\ddot{\xi} + C(\xi, \dot{\xi})\dot{\xi} + g(\xi) = \tau_c + \tau_e \quad (7)$$

where $M(\cdot)$ is the state-dependent inertia matrix, $C(\cdot)$ is a matrix that captures the Coriolis forces, $g(\cdot)$ is the gravity vector, and τ_e refers to external forces interacting with the robot. The passive velocity controller is defined as follows:

$$\tau_c = g(\xi) - D(\xi)(\dot{\xi} - f(\xi^*)), \quad \dot{\xi}^* = f(\xi^*) \quad (8)$$

where $D(\cdot)$ is a damping term to induce passivity, and $f(\cdot)$ is a simple linear dynamic system tracking the target ξ^* received from the filtering pipeline. This controller formulation allows humans to push the robot without causing an antagonistic reaction, although no collision occurred. The HPE backbone, the tracking target node, and the velocity controller are kept fixed during all the experiments.

B. Participants

A total of 7 adults participated in the experiments (28.5% female (n=2), 71.5% male(n=5)). The mean age of the participants was 25.8 years (SD=1.94). The participants were predominantly right-handed, 85.7% (n=6) and 14.3% left-handed (n=1). To simulate experienced operators in an industrial plant, all participants were graduate students with a mechanical engineering background who had previously worked with a robotic manipulator.

C. Tasks

Figure 2 is a graphical representation of the four tasks designed to evaluate the robustness of the proposed pipeline. Each task has an operator O , a human collaborator C , and a robot R . The task of R is to track O_L (i.e., the left hand

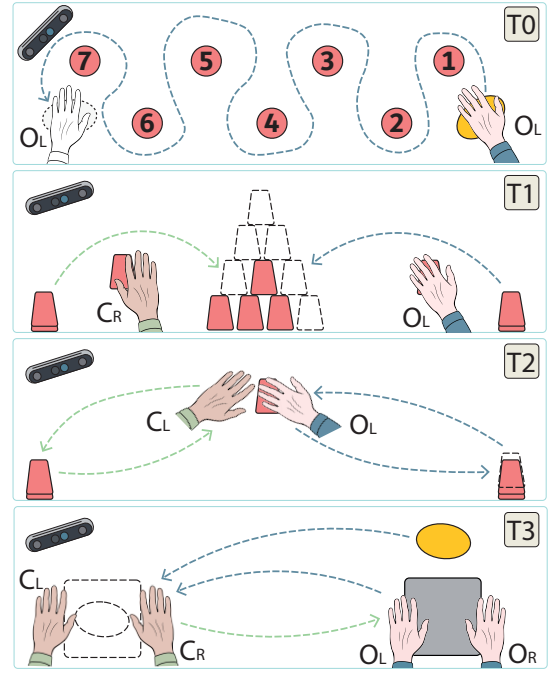


Fig. 2: Visual representations of the four tasks.

of O) at a pre-defined safety distance of 150mm along the x and z axes. In particular, the tasks are:

- **T0:** O_L moves a small object from O 's right side to the left, avoiding obstacles in a sinusoidal pattern. C is not involved but is still visible during the entire task. This task is designed to test the filter capability in non-linear movements.
- **T1:** O_L and C_R (i.e., C 's right hand) collaboratively place 10 cups on each other to form a pyramid. They start with 5 cups each and are not instructed on how to form the pyramid. We designed this task to test the influence of the interaction between O_L and C_R .
- **T2:** O_L picks up 5 cups and hands them over to C_L , one at a time. Once the first handover is complete, the task is repeated in the other direction (from C_L to O_L). This task is designed to test the robustness of the filters when O_L and C_L are very close.
- **T3:** O picks up a box with both O_L and O_R , handing it over to C . While C opens the box, O_L picks and hands over an object to C_R . Then, C_R places the object in the box, C closes it, and hands it back to O . We designed this task to test the filter's efficacy in detecting the occlusion of O_L during the heavy handover.

D. Baselines and implementation details

We compared our filter with two widely used implementations of the Linear Kalman filter. The first motion model follows first-order dynamics (*1st*) with constant velocity. The second motion model follows second-order dynamics (*2nd*) with constant acceleration. The rest of the parameters are set as in [31].

We found the optimal values for each parameter through grid search and then fixed them throughout the experiments.

TABLE I: Tracking quality assessment measuring Mean Absolute Error (MAE), Standard Deviation of the Euclidean Distance (STD), and Mean Acceleration Error (ACC). The average computation time of each filter is expressed in *ms*.

Tasks Evaluation Metrics	T0			T1			T2			T3			avg time (<i>ms</i>)
	MAE (<i>mm</i>)	STD (<i>mm</i>)	ACC (<i>m/s²</i>)	MAE (<i>mm</i>)	STD (<i>mm</i>)	ACC (<i>m/s²</i>)	MAE (<i>mm</i>)	STD (<i>mm</i>)	ACC (<i>m/s²</i>)	MAE (<i>mm</i>)	STD (<i>mm</i>)	ACC (<i>m/s²</i>)	
Baseline	66.69	163.15	12.65	195.07	271.69	11.83	147.39	173.12	11.88	319.25	257.59	11.72	-
Kalman Filter (1st)	69.57	127.88	6.94	149.52	215.98	6.43	227.56	192.59	7.27	315.66	262.06	8.20	2.95
Kalman Filter (2nd)	64.19	122.18	6.63	163.28	192.8	6.75	149.35	147.12	6.54	258.13	241.96	7.71	3.01
Ours	48.89	19.55	7.24	96.98	79.37	8.86	81.62	68.12	6.07	77.47	83.83	7.57	8.22

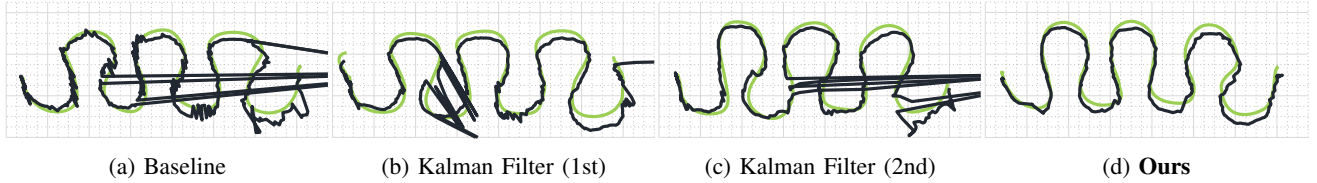


Fig. 3: 2D projection on the XY axis of the task T0. In green is the wrist position captured by the ground truth, in black the compared marker-less methods: OpenPose [20] without filters (a), OpenPose filtered by Kalman filter of the first order (b), second order (c) and our filter (d).

In the spatial evaluation node, the distance threshold Δ is set to 3.0 m, and both the reward factor r and the penalty function p are set to 10%. The step constant δ is set to 0.5 in the temporal evaluation node. In the permanence filter, we assume first-order polynomial dynamics for f . For the observation covariance noise R , α is set to 0.01 and β is set to 0.2. The occlusion threshold T is set to 0.4, and the size of the dynamic module’s past trajectory γ is set to 50 frames.

E. Evaluation metrics

We compared the output of the *tracking target node* with the ground truth obtained from the marker-based motion capture system. We quantified the quality of the tracking with three metrics:

- **MAE**: it is the average of the Euclidean distances between the two 3D trajectories
- **STD**: it is the standard deviation of the Euclidean distances between the two 3D trajectories
- **ACC**: it is the average of the Euclidean distances between the second derivatives of the two 3D trajectories

We also collected the end-effector’s position to quantify compliance with the predefined safety distance, defined as the standard deviation of the Euclidean distances between O_L and the end-effector. We collected participants’ feedback through a survey. Before beginning the study, we did not inform the operator about the filtering methods. For each task, we ran the compared methods in random order. After each task, participants rated the following question: “How safe did you feel during this task?” on a Likert scale to quantify the perceived safety. We performed a one-way ANOVA and then the Tukey-Kramer test to identify statistically significant differences between the methods’ mean ratings.

IV. RESULTS

Table I compares our filter with the baseline and the other filters. On average, our method improved the MAE of the

TABLE II: Safety distance compliance measuring the standard deviation of the distance between end-effector and wrist.

Tasks	T0	T1	T2	T3
Baseline	171.42	161.72	95.37	121.23
Kalman Filter (1st)	139.4	115.71	98.65	119.24
Kalman Filter (2nd)	144.5	104.17	80.08	103.91
Ours	118.84	46.58	44.66	86.78
Marker-based	113.64	33.99	42.4	77.93

baseline by 49.33% (105.86mm), outperforming 1st and 2nd order Kalman filters by 51.11% (114.33mm) and 44.94% (82.49mm), respectively. Also, STD was reduced similarly. On average, our approach showed a 71.72% (153.67mm) decrease in STD w.r.t. the baseline, and outperformed the 1st and 2nd order Kalman filters by 70.15% (136.91mm) and 65.47% (13.29mm), respectively. We then observed a 38.04% (4.58 m/s^2) reduction in ACC compared to the baseline, achieving comparable performance to Kalman filters designed to provide smooth behavior. On average, our method’s computation time is negligible and comparable to the other tested methods.

Table II shows the standard deviation of the distance between the robot end-effector and O_L . From this perspective, our filter is almost as consistent as the ground truth (only 14.57% (7.22mm) higher). Table III assesses participants’ perceptions of safety during the experiments. The results indicated a notable increase in perceived safety and comfort when interacting with the robot using our proposed method (4.6/5 vs 2.2/5). The Tukey-Kramer test proved statistically significant differences between our method and the others.

For qualitative inspection, Figure 3 shows the 2D projection of O_L during task T0. By minimizing the jitter and large errors caused by occlusions and false predictions and tracking errors, our method produces qualitatively superior results. Since the trajectories of the other three tasks are too

TABLE III: Perceived safety by the participants on a Likert scale and statistical difference from the baseline (pval < 0.05), along with Lower Confidence Interval (LCI) and Upper Confidence Interval (UCI).

Tasks	T0	T1	T2	T3	diff (LCI, UCI)
Baseline	2.1	1.2	1.8	1.7	-
Kalman Filter (1st)	2.6	2.3	2.7	2.2	+1.3 (+0.1, +0.7)
Kalman Filter (2nd)	3.1	2.3	2.7	2.3	+1.5 (+0.2, +0.8)
Ours	4.7	4.3	4.7	4.5	+3.5 (+2.1, +2.8)

complex to represent in 2D, we provide a qualitative video in the supplementary materials.

V. CONCLUSION

Traditional marker-based motion capture systems, while offering high accuracy, are often impractical for everyday use due to their overhead and cost. Markerless motion tracking offers a promising solution for more natural and unobtrusive interactions. However, existing methods face accuracy challenges when dealing with complex scenarios such as occlusions and multi-person interactions. To address these limitations, we proposed a novel filtering pipeline that improved the reliability of any HPE in multi-person HRI environments. Our experimental results demonstrated the effectiveness of the filter in various real-world tasks, outperforming traditional tracking algorithms in terms of safety, smoothness, and user comfort.

REFERENCES

- [1] L. S. Scimmi, M. Melchiorre, S. Mauro, and S. P. Pastorelli, "Implementing a vision-based collision avoidance algorithm on a ur3 robot," in *2019 23rd International Conference on Mechatronics Technology (ICMT)*, 2019, pp. 1–6.
- [2] I. Cerulo, F. Ficuciello, V. Lippiello, and B. Siciliano, "Teleoperation of the schunk s5fh under-actuated anthropomorphic hand using human hand motion tracking," *Robotics and Autonomous Systems*, vol. 89, pp. 75–84, 2017.
- [3] M. Field, D. Stirling, F. Naghdy, and Z. Pan, "Motion capture in robotics review," in *2009 IEEE International Conference on Control and Automation*, 2009, pp. 1697–1702.
- [4] K. Lockwood, G. Streng, Y. Bicer, T. Imbiriba, M. P. Furmanek, T. Padir, D. Erdogmus, E. Tunik, and M. Yarossi, "Gaussian process-based prediction of human trajectories to promote seamless human-robot handovers," in *2023 32nd IEEE International Conference on Robot and Human Interactive Communication (RO-MAN)*. IEEE, 2023, pp. 2259–2266.
- [5] G. Nagymáté and R. M. Kiss, "Application of optitrack motion capture systems in human movement analysis: A systematic literature review," *Recent Innovations in Mechatronics*, vol. 5, no. 1, p. 1–9., Apr. 2018.
- [6] S. L. Colyer, M. Evans, D. P. Cosker, and A. I. T. Salo, "A review of the evolution of vision-based motion analysis and the integration of advanced computer vision methods towards developing a markerless system," *Sports Medicine - Open*, 2018.
- [7] C. Zheng, W. Wu, C. Chen, T. Yang, S. Zhu, J. Shen, N. Kehtarnavaz, and M. Shah, "Deep learning-based human pose estimation: A survey," *ACM Computing Surveys*, vol. 56, no. 1, pp. 1–37, 2023.
- [8] G. Du and P. Zhang, "Markerless human-robot interface for dual robot manipulators using kinect sensor," *Robotics and Computer-Integrated Manufacturing*, vol. 30, p. 150–159, 04 2014.
- [9] H. Liu and L. Wang, "Gesture recognition for human-robot collaboration: A review," *International Journal of Industrial Ergonomics*, vol. 68, pp. 355–367, 2018.
- [10] J.-H. Park, Y.-D. Shin, J.-H. Bae, and M.-H. Baeg, "Spatial uncertainty model for visual features using a kinect™ sensor," *Sensors*, vol. 12, no. 7, pp. 8640–8662, 2012.
- [11] D. Wei, L. Chen, L. Zhao, H. Zhou, and B. Huang, "A vision-based measure of environmental effects on inferring human intention during human robot interaction," *IEEE Sensors Journal*, vol. 22, no. 5, pp. 4246–4256, 2021.
- [12] M. S. Yasar, M. M. Islam, and T. Iqbal, "Posetron: Enabling close-proximity human-robot collaboration through multi-human motion prediction," in *Proceedings of the 2024 ACM/IEEE International Conference on Human-Robot Interaction*, ser. HRI '24. ACM, Mar. 2024.
- [13] A. Kothari, T. Tohme, X. Zhang, and K. Youcef-Toumi, "Enhanced human-robot collaboration using constrained probabilistic human-motion prediction," 2023.
- [14] T. Wang, P. Zheng, S. Li, and L. Wang, "Multimodal human-robot interaction for human-centric smart manufacturing: A survey," *Advanced Intelligent Systems*, p. 2300359, 2023.
- [15] M. Lorenzini, M. Lagomarsino, L. Fortini, S. Gholami, and A. Ajoudani, "Ergonomic human-robot collaboration in industry: A review," *Frontiers in Robotics and AI*, vol. 9, Jan. 2023.
- [16] D. Sirintuna, A. Giammarino, and A. Ajoudani, "Human-robot collaboration carrying of objects with unknown deformation characteristics," *CoRR*, vol. abs/2201.10392, 2022.
- [17] M. Dagioglou, A. C. Tsitos, A. Smarnakis, and V. Karkaletsis, "Smoothing of human movements recorded by a single rgb-d camera for robot demonstrations," in *Proceedings of the 14th PErvasive Technologies Related to Assistive Environments Conference*, 2021, pp. 496–501.
- [18] R. Takamido and J. Ota, "Learning robot motion in a cluttered environment using unreliable human skeleton data collected by a single rgb camera," *IEEE Robotics and Automation Letters*, 2023.
- [19] E. Martini, A. Calanca, and N. Bombieri, "Denoising and completion filters for human motion software: a survey with code," *TechRxiv*, May 2023. [Online]. Available: <http://dx.doi.org/10.36227/techrxiv.22956482.v1>
- [20] Z. Cao, T. Simon, S.-E. Wei, and Y. Sheikh, "Realtime multi-person 2d pose estimation using part affinity fields," in *Proceedings of the IEEE conference on computer vision and pattern recognition*, 2017, pp. 7291–7299.
- [21] Y. Zhang, C. Wang, X. Wang, W. Liu, and W. Zeng, "Voxeltrack: Multi-person 3d human pose estimation and tracking in the wild," *IEEE Transactions on Pattern Analysis and Machine Intelligence*, vol. 45, no. 2, pp. 2613–2626, 2022.
- [22] H. Chen, R. Feng, S. Wu, H. Xu, F. Zhou, and Z. Liu, "2d human pose estimation: A survey," *Multimedia Systems*, vol. 29, no. 5, pp. 3115–3138, 2023.
- [23] R. Drillis, R. Contini, and M. Bluestein, "Body segment parameters," *Artificial limbs*, vol. 8, no. 1, pp. 44–66, 1964.
- [24] D. A. Winter, *Biomechanics and motor control of human movement*. John Wiley & sons, 2009.
- [25] H. W. Kuhn, "The hungarian method for the assignment problem," *Naval research logistics quarterly*, vol. 2, no. 1-2, pp. 83–97, 1955.
- [26] X. Weng, J. Wang, D. Held, and K. Kitani, "3d multi-object tracking: A baseline and new evaluation metrics," in *2020 IEEE/RJSJ International Conference on Intelligent Robots and Systems (IROS)*. IEEE, 2020, pp. 10 359–10 366.
- [27] S. Peng, M. X. Wang, J. A. Shah, and N. Figueroa, "Object permanence filter for robust tracking with interactive robots," in *IEEE International Conference on Robotics and Automation (ICRA)*. IEEE, 2024.
- [28] E. Martini, M. Boldo, S. Aldegheri, N. Valè, M. Filippetti, N. Smania, M. Bertuccio, A. Picelli, and N. Bombieri, "Enabling gait analysis in the telemedicine practice through portable and accurate 3d human pose estimation," *Computer Methods and Programs in Biomedicine*, vol. 225, p. 107016, 2022.
- [29] W. Kabsch, "A solution for the best rotation to relate two sets of vectors," *Acta Crystallographica Section A: Crystal Physics, Diffraction, Theoretical and General Crystallography*, vol. 32, no. 5, pp. 922–923, 1976.
- [30] K. Kronander and A. Billard, "Passive interaction control with dynamical systems," *IEEE Robotics and Automation Letters*, vol. 1, no. 1, pp. 106–113, 2016.
- [31] M. MathWorks, "trackingkf," 2023. [Online]. Available: <https://it.mathworks.com/help/driving/ref/trackingkf.html>